AGU PUBLICATIONS

Geophysical Research Letters

RESEARCH LETTER
10.1002/2015GL065385

Key Points:
- Observations of the M_w 7.8 Gorkha, Nepal earthquake and M_w 7.3 aftershock are presented
- ALOS-2 provides burst-aligned ScanSAR interferometry with 350 km swath width
- Data from coseismic and postseismic interferograms are available online for use in modeling studies

Supporting Information:
- Supporting Information S1

Correspondence to:
E. O. Lindsey,
elindsey@ucsd.edu

Citation:
Lindsey, E. O., R. Natsuaki, X. Xu, M. Shimada, M. Hashimoto, D. Melgar, and D. T. Sandwell (2015), Line-of-sight displacement from ALOS-2 interferometry: M_w 7.8 Gorkha Earthquake and M_w 7.3 aftershock, *Geophys. Res. Lett.*, *42*, doi:10.1002/2015GL065385.

Received 14 JUL 2015
Accepted 5 AUG 2015
Accepted article online 9 AUG 2015

Line-of-sight displacement from ALOS-2 interferometry: M_w 7.8 Gorkha Earthquake and M_w 7.3 aftershock

Eric O. Lindsey[1], Ryo Natsuaki[2], Xiaohua Xu[1], Masanobu Shimada[2], Manabu Hashimoto[3], Diego Melgar[4], and David T. Sandwell[1]

[1]Institute for Geophysics and Planetary Physics, University of California, San Diego, San Diego, California, USA, [2]Earth Observation Research Center, Japan Aerospace Exploration Agency, Tsukuba, Japan, [3]Disaster Prevention Research Institute, Kyoto University, Kyoto, Japan, [4]Seismological Laboratory, University of California, Berkeley, California, USA

Abstract Interferometric synthetic aperture radar (InSAR) is a key tool for the analysis of displacement and stress changes caused by large crustal earthquakes, particularly in remote areas. A challenge for traditional InSAR has been its limited spatial and temporal coverage especially for very large events, whose dimensions exceed the typical swath width of 70–100 km. This problem is addressed by the ALOS-2 satellite, whose PALSAR-2 instrument operates in ScanSAR mode, enabling a repeat time of 2 weeks and a swath width of 350 km. Here we present InSAR line-of-sight displacement data from ALOS-2/PALSAR-2 observations covering the M_w 7.8 Gorkha, Nepal earthquake and its M_w 7.3 aftershock that were acquired within 1 week of each event. The data are made freely available and we encourage their use in models of the fault slip and associated stress changes. The M_w 7.3 aftershock not only extended the rupture area of the main shock toward the east but also left a 20 km gap where the fault has little or no coseismic slip. We estimate this unslipped fault patch has the potential to generate a M_w 6.9 event.

1. Introduction

The M_w 7.8 Gorkha, Nepal earthquake and M_w 7.3 aftershock struck in a region with less than optimal seismic and geodetic coverage [e.g., *Ader et al.*, 2012]. The moment tensor solution based on far-field seismic stations combined with the tectonics of the region suggests thrust faulting on a shallow dipping fault (11°) having a strike of 295° [*U.S. Geological Survey (USGS)*, 2015]. Initial finite fault models based on methods of *Ji et al.* [2002] show 2–4 m of slip at ~15 km depth over a zone extending ~150 km ESE of the hypocenter. The earthquake caused intense ground shaking throughout much of Nepal and parts of India and China, resulting in over 8000 deaths. Ground shaking in the Kathmandu basin was particularly intense as a result of its proximity to the main rupture area and the effects of basin amplification and directivity, causing many historical structures to collapse that had survived previous earthquakes [*USGS*, 2015, *Galetzka et al.*, 2015].

Several interferometric synthetic aperture radar (InSAR) satellites were operational at the time of the earthquake and continue to collect measurements of line-of-sight (LOS) displacement. The Sentinel-1a satellite, operated by the European Space Agency (ESA) collected C-band InSAR observations, which were processed and made available online by the ESA Scientific Exploitation of Operational Missions project (SEOM—http://insarap.org). The ALOS-2 satellite, operated by the Japan Aerospace Exploration Agency (JAXA), collected L-band InSAR data, low-resolution images of which are presented at the JAXA site (http://www.eorc.jaxa.jp/ALOS/en/) as well as the Geospatial Information Authority of Japan (GSI—http://www.gsi.go.jp/cais/topic150429-index-e.html).

This study is focused on the extraction of LOS displacement from the ALOS-2/PALSAR-2 instrument, with the objective of providing these observations to the modeling community, as the raw data are not freely available and this is the first publication of ALOS-2 ScanSAR InSAR. Rapid assessment of the acquired data is also important for scheduling of future acquisitions. ALOS-2 operates in several modes, including traditional strip-mode SAR with a swath width of 70 km, and ScanSAR (Wide Swath), with a width of 350 km. Although wide swath data are desirable due to the larger image size, most interferograms are constructed from strip-mode data and ScanSAR-to-ScanSAR interferometry is rare because it requires accurate burst alignment between the reference and repeat orbit. This implies precise on-board timing to better than 70 ms. This was first achieved with the ALOS-1 satellite in cases where the bursts were aligned by chance [*Tong et al.*, 2010]. ALOS-2 is the first L-band satellite to offer burst-aligned ScanSAR interferometry as a standard operating mode, but during the commissioning of the satellite it was discovered that

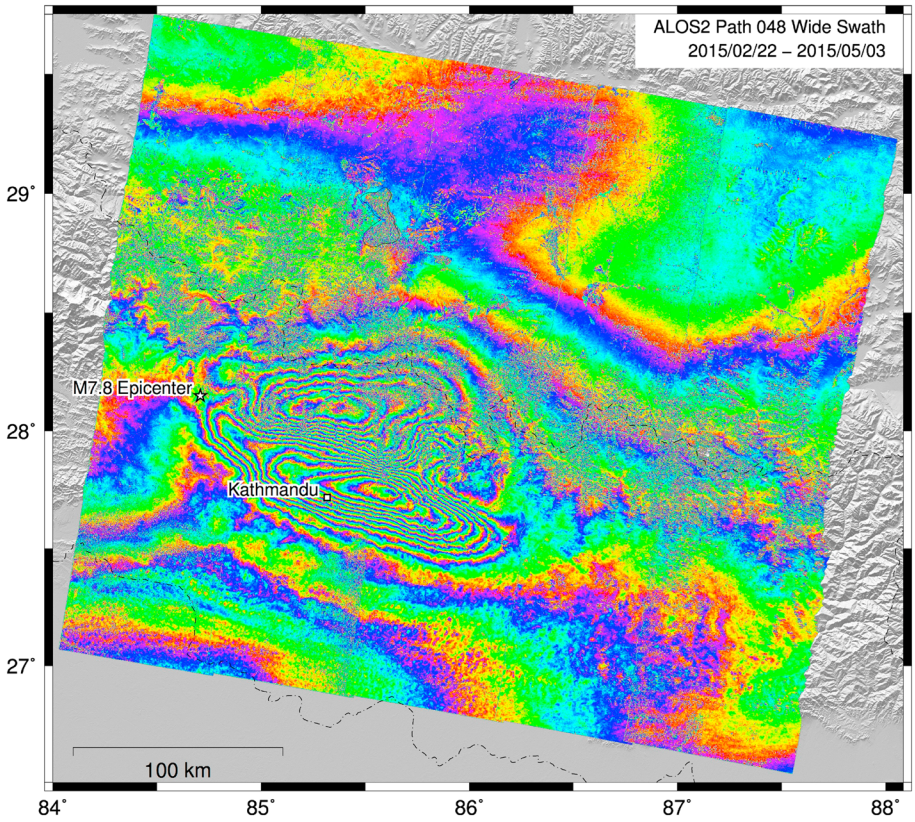

Figure 1. Example of a coseismic ScanSAR-to-ScanSAR interferogram from ALOS-2 descending Path 48, spanning dates 22 February 2015 to 3 May 2015 and covering the M_w 7.8 Gorkha, Nepal earthquake. Each color cycle (red-green-blue-red) represents 12.1 cm of displacement toward the satellite. Data were processed using GMTSAR [*Sandwell et al.*, 2011]. Note that ALOS-2 provides continuous phase across subswath boundaries with no adjustment resulting in a single 350 km by 350 km interferogram.

the burst alignment was inconsistent. The problem was corrected on 8 February 2015, 11 weeks prior to the *M*7.8 rupture, and thus, the quality of the ScanSAR interferograms was not completely understood at the time of the main shock. Below, we demonstrate that the burst alignment problem was indeed corrected; a more detailed analysis of the issue is included in Appendix A. ScanSAR-to-ScanSAR interferograms (Figure 1) provide an accurate and complete mapping of the surface displacement of these two major earthquakes, which occurred in a region with the greatest topographic relief on Earth.

This manuscript describes the new data and processing methods and more importantly refers to a web site where we present line-of-sight (LOS) data files for each track and frame described here for use in modeling studies [e.g., *Wang and Fialko*, 2015; *Galetzka et al.*, 2015]. We will continue to provide postseismic LOS data as they become available. The data were processed with an updated version of GMTSAR software [*Sandwell et al.*, 2011] with additional post processing using GMT [*Wessel et al.*, 2013] and SNAPHU [*Chen and Zebker*, 2000]. The details of the processing are described in Appendix B. The results show continuous phase across the subswath boundaries and demonstrate that the PALSAR-2 radar provides spatially consistent phase over the entire region (Figure 1).

2. Line-of-Sight Displacement

ALOS-2 InSAR coverage of the M_w 7.8 and M_w 7.3 ruptures is excellent. Each rupture was independently imaged from both the ascending and descending look directions (Figures 2 and 3). Coherence is maintained except in areas of very steep topography or snow cover. A close inspection of the main shock interferograms (Figures 2a and 3a) shows no major discontinuities in phase near the surface trace of the Main Himalayan Thrust (MHT). Indeed, the surface displacement field is smooth and consistent with the majority of slip

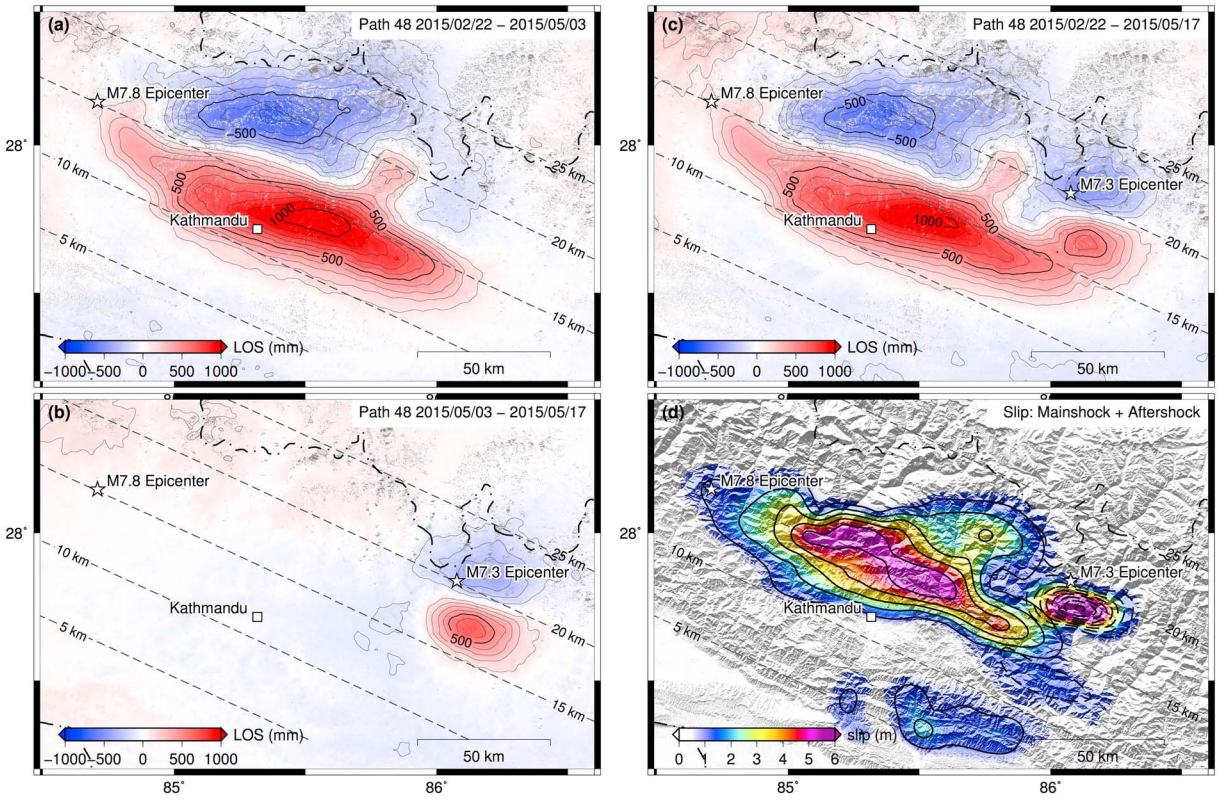

Figure 2. LOS displacement in millimeters for subarea covered by ALOS-2 along descending Path 48. Dashed lines show depth to fault plane, from the USGS W-phase moment tensor solution nodal plane [*USGS*, 2015]. (a) LOS displacement for a time interval spanning the M_w 7.8 earthquake. This represents mainly vertical motion with a trough-to-peak amplitude of ~1.6 m. (b) LOS displacement for a time interval spanning the M_w 7.3 aftershock. The trough-to-peak amplitude is ~1.1 m. (c) LOS displacement for a time interval spanning both events. The overall extent of the combined rupture is ~170 km. (d) Slip inversion of the LOS data from Paths 48 and 157 based on the modeling approach of *Melgar and Bock* [2015]. Maximum slip is ~ 6 m. The shallow (<10 km) slip feature is preferred by data from Path 157 but does not appear to be required by the Path 48 data (see Figures S2 and S3 in the supporting information). There is a notable gap in slip centered approximately 20 km to the west of the M_w 7.3 aftershock hypocenter.

occurring between 10 and 20 km depth, with virtually all slip to the East of the hypocenter. Since the LOS vector from the descending pass (Path 48) is nearly parallel to the strike of the MHT, the LOS motion primarily reflects vertical deformation caused by a large amount of slip on a shallow dipping fault. In contrast, the LOS vector from the ascending pass (Path 157) is at about a 30° angle from the strike of the fault so it records a larger LOS displacement (Figure 3a). Preliminary modeling (below) suggests that the maximum fault slip lies between the maximum and minimum lobes in the LOS displacement, at a depth of about 15 km.

The LOS displacement from the M_w 7.3 aftershock shows a pattern that is similar, but more compact, than the displacement from the main shock (Figures 2b and 3b). As in the case of the main shock, the trough-to-peak displacement of the aftershock is larger along the ascending track than it is along the descending track, in agreement with a slip vector oriented along dip. The low-to-high gradient in the displacement of the aftershock is larger than the main shock suggesting there is a slip concentration at depth. Most of the displacement from the M_w 7.3 aftershock occurs near the eastern end of the displacement from the main rupture suggesting it may have been triggered by a Coulomb stress concentration from the main shock [*Galetzka et al.*, 2015].

To better understand how the surface displacements relate to slip at depth, we inverted the LOS displacements for descending and ascending tracks for both main shock and aftershock. We used the 1-D layered Earth structure and inversion method of *Melgar and Bock* [2015]. We assume a planar fault derived from the nodal plane of a W-phase moment tensor inversion [*USGS*, 2015] with a strike of 295° and a dip of 11°. For the main shock we discretized the dislocation surface into 10 × 10 km subfaults, and for the aftershock into 5 × 5 km subfaults. The LOS measurements are downsampled using the QuadTree technique [*Lohman and Simons*, 2005]; the distribution of downsampled data and residuals are shown in Figure S1 in the supporting information. The inverse problem is ill posed, so the inversion is regularized by applying minimum norm smoothing. The regularization parameter, which limits the level of roughness, is objectively selected by using

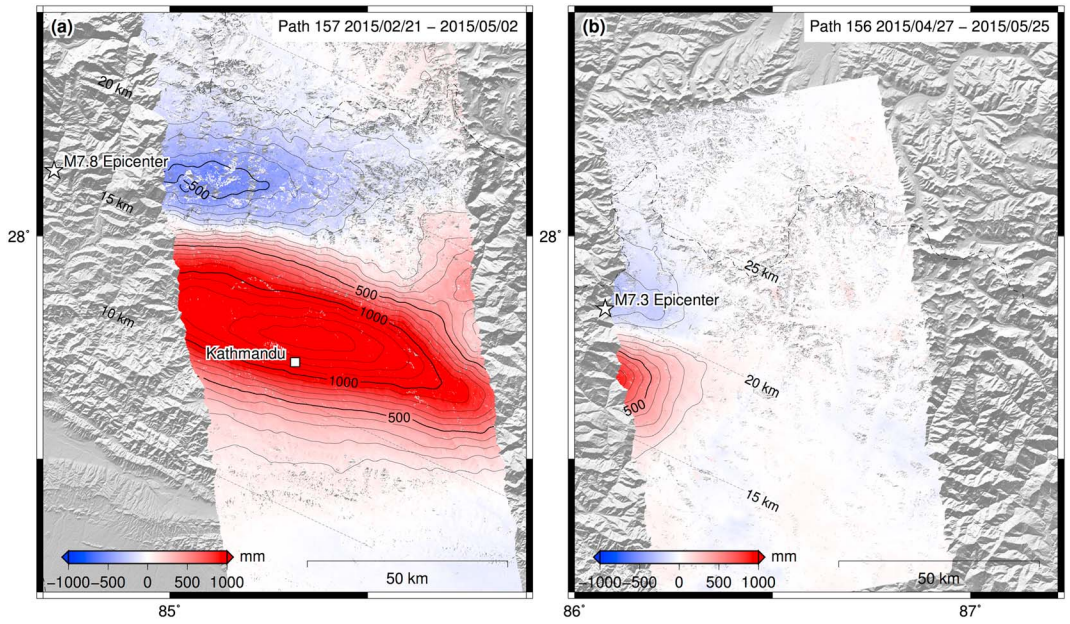

Figure 3. LOS displacement in millimeters from ALOS-2 along ascending paths. Dashed lines show depth to fault plane. (a) LOS displacement on path 157 spanning the M_w 7.8 earthquake has a trough-to-peak displacement of ~2.1 m. (b) LOS displacement on path 156 spanning the M_w 7.3 earthquake has a trough-to-peak displacement of ~1.1 m.

Akaike's Bayesian Information Criterion [*Yabuki and Matsu'Ura*, 1992]. We assume uniform uncertainties for the InSAR data, which therefore do not affect the regularization. We consider the effect of inverting for slip using only the descending or ascending tracks individually in Figure S2, and the effect of choosing a higher or lower penalty on the model norm (greater or lesser smoothing) in Figure S3.

The results are shown in Figure 2d. Main shock slip extends over an area ~170 km long and between the 5 to 15 km depth contours, with peak slip of 5.5–6.5 m over a large asperity just north of Kathmandu. Peak slip depends somewhat on the choice of regularization; see Figure S3. Peak slip for the aftershock may be slightly larger but is less well constrained (5.5–10 m, depending on the regularization) and is concentrated on a very compact asperity about 30 km in length. The aftershock slip area shows little to no overlap with the main shock slip. Notably, there is an area of little or no slip at 15–20 km depth between the two events. This gap appears to be well constrained by the data irrespective of the value of the regularization parameter (Figure S3).

3. Discussion and Conclusions

The displacement field for the interferogram and derived slip inversions spanning both the main shock and aftershock show an interesting pattern. While the aftershock extended the rupture area of the main shock toward the east, it did not completely fill the "gap" formed by the NE trending tongue in high slip. Thus, a large (20 km) area remains where the fault has little or no coseismic slip (Figure 2d). By scaling the area of the displacement field from the M_w 7.3 rupture to the area of the unruptured zone, we estimate this unslipped fault patch has the potential to generate a M_w 6.9 event. Furthermore, the tongue of surface displacement maps to a smaller asperity in the main shock slip pattern at 20–25 km depth. If this represents the down dip edge of the seismogenic zone, then there is potential for further slip down dip of the patches broken thus far. It will be important to monitor this slip gap over the coming years, a task that will be aided by the recently installed continuous GPS site GUMB (John Galetzka, personal communication, 2015). If ALOS-2 continues operating in the ScanSAR mode along path 048 with a 14 to 42 day repeat, it will be possible to acquire a complete space-time map of this and other regions surrounding the rupture zone.

The ScanSAR InSAR capabilities of ALOS-2 prove to be a capable tool for monitoring large continental earthquakes such as the Nepal sequence. The Himalayan region has the largest relief on the Earth, is densely vegetated, and has snow-capped peaks. The L-band radar enables adequate InSAR correlation in the vegetated areas, while tight baseline control of the spacecraft to better than 120 m in these examples

minimizes the unwanted phase due to errors in the extreme topography. Finally, the onboard navigation is now accurate enough to provide better than 70% overlap of the ScanSAR bursts between reference and repeat images. This results in single interferograms 350 km wide that are able to completely image the deformation resulting from these major events. This wide swath also enables a short 14 day repeat interval that was able to collect images between the M_w 7.8 and M_w 7.3 events. Slip models based on the deformation spanning the M_w 7.8 event can be used to estimate the Coulomb stress that may have triggered the M_w 7.3 event. The slip gap observed between the two ruptures (Figure 2d) can now be monitored for coseismic slip or aseismic creep. Finally, the large vertical displacement caused by this thrust event will also induce significant viscoelastic deformation over the next years to decades that we hope will be accurately imaged and modeled.

Appendix A: Burst Alignment

ALOS-2 is the first L-band SAR with routine InSAR acquisitions in the ScanSAR mode [*Kankaku et al.*, 2009]. The interferometric wide mode (WD1) has five subswaths to achieve an overall ground swath width of 350 km, with characteristics provided in Table S1 in the supporting information. The wide swath makes it possible to completely image an area every 14 days instead of the 42 day repeat interval that is needed for complete imaging in swath mode. There are two basic requirements for achieving accurate displacement maps from normal strip-mode InSAR. First the along-track Doppler spectra of the reference and repeat images should have more than about 50% overlap. Second, the perpendicular baseline distance between the reference and repeat acquisitions should be smaller than about 20% of the critical baseline. ALOS-2 is well within these limits so one can construct high-quality strip-mode interferograms from all the acquisitions. However, construction of high-quality ScanSAR to ScanSAR interferograms also requires that the bursts have more than 50% overlap on the ground. Poor quality interferograms can be achieved when the burst overlap is as small as 20%.

To achieve this burst overlap the radar system must be triggered with an along-track accuracy better than ~500 m, which corresponds to a timing accuracy better than 70 ms [*Tong et al.*, 2010]. The autonomous navigation system aboard ALOS-2 was designed to achieve horizontal baseline better than 500 m and along-track accuracy of 10 m [*Kankaku et al.*, 2009]. During the commissioning phase of the mission, accurate baseline control was demonstrated with most perpendicular baselines less than 200 m. However, the initial interferograms usually had no burst overlap. JAXA implemented an adjustment to the onboard navigation system in early February 2015 and adequate burst overlap has been maintained since then. The first pass after the 8 February fix and prior to the Nepal earthquakes was P048 on 22 February. Subsequent pairs have burst overlap better than 70%, as listed in Table A1.

We performed a systematic analysis of the burst overlap between acquisitions from before and after 8 February 2015 for 10 different locations worldwide, the results of which are listed in Table S2 in the supporting information. We found an approximately 365 day sinusoidal oscillation in the burst overlap (Figure A1). The amplitude of the oscillation is greater than the 2100 pixel burst spacing, so the values are wrapped onto the range (−1050, 1050). We fit a model of the form:

$$B(D) = \mathrm{mod}\{A\sin[2\pi(D - D_o)/T] + 1050, 2100\} - 1050 \quad \text{(A1)}$$

where B is the burst offset at day D, in days relative to date D_0. The best fitting parameters are amplitude $A = 3635$ pixels, period $T = 365$ days, and zero phase date $D_0 = 20$ December 2014.

Table A1. Interferograms Used in This Study[a]

Track Mode	Reference Date Product	Repeat Date Product	B. perp. (m)	Az. shift (pixel)	Burst Overlap	Mean Coherence
T048 ScanSAR	22 Feb 2015 ALOS2040533050-150222	5 Apr 2015 ALOS2046743050-150405	43.7	−18	95%	0.33
T048 ScanSAR	22 Feb 2015 ALOS2040533050-150222	03 May 2015 ALOS2050883050-150503	48.0	−106	72%	0.20
T048 ScanSAR	05 Apr 2015 ALOS2046743050-150405	03 May 2015 ALOS2050883050-150503	4.3	−84	78%	0.27
T048 ScanSAR	03 May 2015 ALOS2050883050-150503	17 May 2015 ALOS2052953050-150517	−97.7	3	99%	0.43
T047 ScanSAR	31 Mar 2015 ALOS2046003050-150331	28 Apr 2015 ALOS2050143050-150428	81.0	−91	76%	0.25
T157 Swath	21 Feb 2015 ALOS2040460540-150221	2 May 2015 ALOS2050810540-150502	−118.6	−3	N/A	0.23
T156 Swath	27 Apr 2015 ALOS2050070550-150427	25 May 2015 ALOS2054210550-150525	−39.9	−2	N/A	0.29

[a]ScanSAR burst overlap is computed according to the formula 100 × (nburst − az. shift)/nburst, using nburst for subswath 3 from Table S1. B. perp. denotes the perpendicular baseline between orbits; Az. shift is the along-azimuth shift in pixels between corresponding bursts in the two images.

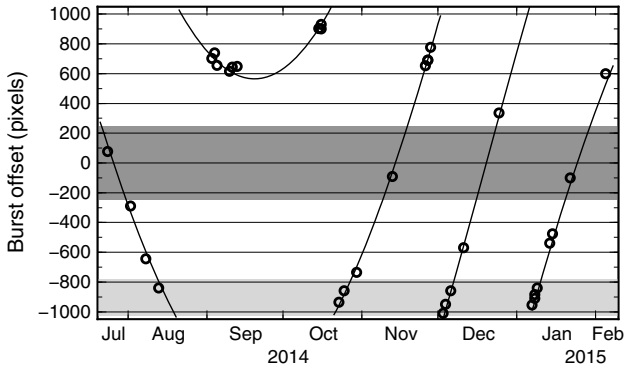

Figure A1. Burst offset versus time for subswath 1. Other subswaths follow the same pattern with a different *y* axis scale. Circles are the observed burst offset between pre- and post-8 February 2015 acquisitions at 10 different locations worldwide (values are provided in Table S2). The modeled curve was computed using equation (A1). Dark grey box shows acquisitions that have a 95% chance of at least 20% burst overlap with post-8 February data. Lighter grey box shows some example acquisitions that have at least 20% burst overlap only with each other.

Equation (A1) can be used to predict interferometric pairs that are likely to have better than 20% burst overlap. In Figure A1, the dark grey box centered at 0 burst offset shows the dates of acquisitions with a 95% chance of more than 20% burst overlap with acquisitions after 8 February. The corresponding date ranges are 22–31 July, 8–17 November, 16–23 December, and 20–29 January. The lighter grey box centered at a burst offset of −900 shows an example of acquisitions that will correlate with each other but not with acquisitions after 8 February.

Appendix B: InSAR Processing and Phase Unwrapping

The ALOS-2 PALSAR-2 data were processed using an updated version of the GMTSAR software [*Sandwell et al.*, 2011] and the phase was unwrapped using SNAPHU software [*Chen and Zebker*, 2000]. Interferograms used are given in Table A1. In all cases we started with the Single Look Complex (SLC, L1.1) products with HH polarization, in CEOS format as delivered from the ALOS User Interface Gateway (https://auig2.jaxa.jp/ips/home). For the ScanSAR processing we began with the full aperture product. The ScanSAR interferograms were low-pass filtered with a 0.5 gain at 500 m wavelength while a 200 m low-pass filter was applied to the strip-mode data. Our strategy is to process each frame (along track) or subswath (across track) independently in radar coordinates and assemble them in geographic coordinates. We have found that phase will be nearly continuous across subswath boundaries if an identical orbit and geometric model is used for all the components [*Tong et al.*, 2010]. The small phase mismatch at the boundaries depends on the method used to align the reference and repeat images. The geometric and orbital errors should only introduce an offset and stretch in both the range and azimuth coordinates, which corresponds to estimating four parameters when fitting the subwindow cross correlation peaks. Because of ionospheric distortions in azimuth, we also solve for an additional parameter that corresponds to the stretch in azimuth as a function of azimuth, resulting in a five-parameter model. If six or more parameters are used, the coherence of the interferogram will increase slightly but the phase will have a significant mismatch on frame or subswath boundaries.

We unwrapped each frame or subswath independently in radar coordinates using SNAPHU software [*Chen and Zebker*, 2000] with an improved algorithm for masking of decorrelated areas [*Agram and Zebker*, 2009]. We then geocoded the results and combined the subswaths into a single interferogram by adding a multiple of 2π to achieve matching phase at the boundaries. For several of the subswaths there was also a phase discontinuity across the snow-covered Himalaya Mountains. Again, a multiple of 2π was added to the area of discontinuous phase to bring it into accordance with the multisubswath interferogram. After correcting the integer unwrapping errors, the frames or subswaths were combined using the GMT function grdblend, which provides seamless blending in overlap areas. The final unwrapped phase was converted to line-of-sight (LOS) displacement using the appropriate center wavelength. Several of the interferograms have large phase ramps related to orbit error and/or ionospheric delays. We remove a ramp from the composite LOS data by estimating a gradient far from the earthquake displacement; LOS data with no trend removed are also provided. Data are median filtered onto 1 km posting and are provided in an ASCII file containing: longitude, latitude, elevation, look vector, LOS (mm), and uncertainty. In addition, the GMT-format NetCDF grid files of geolocated LOS displacements and satellite look vectors at 90 m posting are also available. All results are available at http://topex.ucsd.edu/nepal and will be archived at UNAVCO.

Acknowledgments
We thank JAXA for rapid acquisition and distribution of the ScanSAR data especially along track 048. The data were provided under PI investigations 1148: Geometric and Interferometric CALVAL of ALOS-2 PALSAR and 1413: Unraveling present-day deformation around the eastern and western syntaxes of the Himalayan range. The development of the GMTSAR software and the ALOS-2 preprocessor was supported by ConocoPhillips and the National Science Foundation through the Geoinformatics program (EAR-1347204) and the GeoEarthScope program (EAR-1147435).

The Editor thanks two anonymous reviewers for their assistance in evaluating this paper.

References

Ader, T., et al. (2012), Convergence rate across the Nepal Himalaya and interseismic coupling on the Main Himalayan Thrust: Implications for seismic hazard, *J. Geophys. Res.*, *117*, B04403, doi:10.1029/2011JB009071.

Agram, P. S., and H. A. Zebker (2009), Sparse Two-Dimensional Phase Unwrapping Using Regular-Grid Methods, *IEEE Trans. Geosci. Remote Sens.*, *6*(2), 327–331, doi:10.1109/LGRS.2009.2012445.

Chen, C. W., and H. A. Zebker (2000), Network approaches to two-dimensional phase unwrapping: Intractability and two new algorithms, *J. Opt. Soc. Am. A*, *17*, 401–414, doi:10.1364/JOSAA.17.000401.

Galetzka, J., et al. (2015), Slip pulse and resonance of Kathmandu basin during the 2015 M_w 7.8 Gorkha earthquake, Nepal imaged with space geodesy, *Science*, doi:10.1126/science.aac6383.

Ji, C., D. J. Wald, and D. V. Helmberger (2002), Source description of the 1999 Hector Mine, California earthquake; Part I: Wavelet domain inversion theory and resolution analysis, *Bull. Seism. Soc. Am.*, *92*(4), pp. 1192–1207, doi:10.1785/0120000916.

Kankaku, Y., Y. Osawa, S. Suzuki, and T. Watanabe (2009), The overview of the L-band SAR onboard ALOS-2, in *Proceedings of Progress in Electromagnetics Research Symposium*, pp. 735–738, The Electromagnetics Academy, Cambridge, Mass.

Lohman, R. B., and M. Simons (2005), Some thoughts on the use of InSAR data to constrain models of surface deformation: Noise structure and data downsampling, *Geochem. Geophys. Geosyst.*, *6*, Q01007, doi:10.1029/2004GC000841.

Melgar, D., and Y. Bock (2015), Kinematic earthquake source inversion and tsunami runup prediction with regional geophysical data, *J. Geophys. Res. Solid Earth*, *120*, 3324–3349, doi:10.1002/2014JB011832.

Sandwell, D. T., R. Mellors, X. Tong, M. Wei, and P. Wessel (2011), Open radar interferometry software for mapping surface deformation, *Eos Trans. AGU*, *92*(28), 234, doi:10.1029/2011EO280002.

Tong, X., D. T. Sandwell, and Y. Fialko (2010), Coseismic slip model of the 2008 Wenchuan earthquake derived from joint inversion of interferometric synthetic aperture radar, GPS, and field data, *J. Geophys. Res.*, *115*, B04314, doi:10.1029/2009JB006625.

U.S. Geological Survey (USGS) (2015), Event page. [Available at http://earthquake.usgs.gov/earthquakes/eventpage/us20002926].

Wang, K., and Y. Fialko (2015), Slip model of the 2015 M_w 7.8 Gorkha (Nepal) earthquake from inversions of ALOS-2 and GPS data, *Geophys. Res. Lett.*, *42*, doi:10.1002/2015GL065201.

Wessel, P., W. H. F. Smith, R. Scharroo, J. F. Luis, and F. Wobbe (2013), Generic Mapping Tools: Improved version released, *Eos Trans. AGU*, *94*, 409–410, doi:10.1002/2013EO450001.

Yabuki, T., and M. Matsu'Ura (1992), Geodetic data inversion using a Bayesian information criterion for spatial distribution of fault slip, *Geophys. J. Int.*, *109*(2), 363–375.